JATIS Journal of Astronomical Telescopes, Instruments, and Systems

RESEARCH PAPER

AstroPIC: architecture overview, science yield modeling, and technology status for the Habitable Worlds Observatory

Dan Sirbu,[a,*] Ruslan Belikov,[a] Eduardo Bendek,[a,b] Kevin Fogarty,[a] Rachel Morgan,[a,b] Kevin Sims,[a] Carson Valdez,[c] Anne Kroo,[c] Olav Solgaard,[c] and David A. B. Miller[c]

[a]NASA Ames Research Center, Moffett Field, California, United States
[b]SETI Institute, Mountain View, California, United States
[c]Stanford University, Ginzton Laboratory, Stanford, California, United States

ABSTRACT. We present the architecture, science yield analysis, and technology status update for "AstroPIC," a near-infrared photonic integrated coronagraph designed for the Habitable Worlds Observatory (HWO). Integrated photonics offer significant advantages for a space-based instrument, including reduced size, weight, and power, as well as high reconfigurability via programmable Mach–Zehnder interferometric (MZI) meshes. We assess the architecture's compatibility with HWO by performing parametric yield studies against current pupil definitions. Our simulations demonstrate that the architecture is robust to segmentation gaps, struts, and secondary obscurations, effectively maintaining exo-Earth yields even in the presence of static aberrations. Complementing these theoretical results, we also collate recent experimental results as part of the "AstroPIC" program that validate key component capabilities. These include a demonstrated monochromatic suppression of 3.5×10^{-10} (94 dB) on chip with a single-input fiber, initial free-space coupling system-level demonstrations, and the fabrication of high-efficiency gratings achieving 81% to 85% component-level grating-coupler efficiency for 20 nm narrowband. We conclude by outlining the status of the technology development program for maturation and consideration for HWO trade studies.

 [DOI: 10.1117/1.JATIS.12.4.041028]

Keywords: astrophotonics; photonic integrated circuits; exoplanets; coronagraphy; high-contrast imaging; wavefront control; Habitable Worlds Observatory; near-infrared channel

Paper 260054 received Feb. 12, 2026; revised May 28, 2026; accepted Jun. 17, 2026; published Jul. 15, 2026.

1 Introduction

The 2020 Decadal Survey for Astrophysics identified the Habitable Worlds Observatory (HWO) as NASA's highest-priority flagship mission following the Roman Space Telescope. Planned for launch in the early 2040s, HWO will perform a direct imaging survey of approximately 100 of the nearest stellar systems and their habitable zones. The primary objective is to detect and perform spectroscopic characterization of around 25 potentially "Earth-like planets" (or "Exo-Earths"). An integrated photonic coronagraph offers a practical means of increasing the mission's scientific return while simultaneously offering a path to reduce certain technical risks for high-contrast

*Address all correspondence to Dan Sirbu, dan.sirbu@nasa.gov

imaging on HWO. Photonic integrated circuits make it possible to add new observing channels and capabilities within the volume, mass, and power constraints of a space telescope.

Photonic integrated circuits (PICs) that employ Mach–Zehnder interferometric (MZI) meshes have emerged as a promising new direction for astrophotonic instrumentation. Their growing significance has been reflected both in the recent literature[1] and in focused discussion forums such as the NASA-hosted Emerging Technologies in Astrophysics Missions workshop.[2] AstroPIC is an integrated photonic coronagraph for HWO that provides key advantages, including reductions in size, weight, and power through miniaturization and reconfigurability through a programmable MZI mesh via controllable phase shifters. In addition, due to its greater flexibility to manipulate light, it can approach theoretical performance limits for coronagraphs and consequently has a greater science yield ceiling. Leveraging industry advancements, commercially available PICs can be either custom-manufactured or part of multiproject wafer runs with continuously improving turnaround times and capabilities that can benefit the design and manufacture of the integrated photonic coronagraph.

We present estimated science yields for key parametric sweeps of the integrated photonic coronagraph, including end-to-end coronagraphic throughput and numbers of channels. The integrated photonic coronagraph is highly reconfigurable and adaptable. We demonstrate its compatibility with the three exploratory analytic concepts (EACs) that have been considered for HWO to date. We present mission yields as parametric sweeps with respect to key pupil parameters, including up to doubling of segment gaps, support struts, and the secondary obscuration diameter. In addition, a reconfigurable photonic coronagraph can be programmed to reject a specific set of modes and thus adapt to stars of different diameters and different telescope instability scenarios. We show the benefits of this through simulations of science yield sensitivities to different levels of aberrations. We demonstrate the benefits of reconfigurability by showing optimized yields when selecting the coronagraphic order. This can be further generalized to perform active wavefront sensing and control directly on the photonic chip; in a traditional coronagraph, this would be performed using a separate deformable mirror (DM).

To provide an overall view of the AstroPIC project's progress, we synthesize key experimental milestones achieved across the Ames and Stanford testbeds. Although component-level characterizations and specific testbed details are reported in companion works, we collate these results here to demonstrate the integrated maturation of the hardware alongside theoretical yield models. Key coronagraphic experimental results include: (1) single-channel input and suppression across a single-output channel measuring 3.5×10^{-10} monochromatic suppression for a nine-channel full upper triangular MZI mesh[3] and (2) experimental demonstration of high-efficiency grating couplers demonstrating 81% to 85% coupling throughput for a 20 nm narrowband.[4] A key simulation result in the companion simulation and theory paper shows that the nine-channel MZI mesh on the manufactured prototype chip enables deep contrast across a 2.5% band on a single mesh. For context, conventional coronagraph testbeds such as the JPL high-contrast imaging testbedtypically achieve broadband performance over ∼10% to 20% bandpasses through achromatic mask design and wavefront-control schemes that operate across multiple wavelength channels. The AstroPIC narrowband result is therefore a component-level demonstration that must be extended through dispersion-engineered couplers and spectral multiplexing of narrowband meshes to reach comparable instrument-level bandwidths and using additional degrees of freedom on the chip, as discussed in Sec. 5.

These recent results highlight the continued maturation of the photonic integrated coronagraph for HWO, showing both the potential for deep suppression possible on-chip, improved coronagraphic throughput, and the potential for utilizing the photonic chip miniaturization advantages for broadband operation. We also provide a roadmap for the development of technology for the photonic coronagraph for HWO.

This paper has a central goal of providing an overview of the AstroPIC concept and the photonic coronagraph's technology development, summarizing key experimental and simulated developments and relevance for the HWO mission. In Sec. 2, we review the top-level architecture of AstroPIC as an NIR coronagraph for HWO and describe at a top level the modeling flow for obtaining science yields. These use photonic coronagraph operators implemented in the coronagraph design survey (CDS) pipeline[5] with yields obtained via the remote server interface dubbed framework for remote implementation of demand-based altruistic yields (FRIDAY) to the altruistic yield optimizer (AYO) design reference mission simulator with the latest parameters relevant for the HWO EACs.[6] In Sec. 3, we summarize parametric studies using yield sensitivities for key telescope pupil parameters, a recent study performed for HWO, including throughput, numbers of channels, sensitivity to static aberrations, and robustness when allowing optimization of the coronagraph configuration for the current stellar observation. We also highlight additional bandwidth optimization made possible through the control of additional degrees of freedom (see simulation-focused companion paper).[7] In Sec. 4, we provide an overview of recent key demonstrations performed at both the Ames and Stanford photonics testbeds. Details about the Ames photonics testbed and experimental results are available in the companion experimental paper.[3] These include demonstrations for a single-channel input channel optimizing suppression in one output channel reaching 3.5×10^{-10} contrast (94 dB) by configuration of the phase shifters along a single diagonal between the input and output, rapidly improving on previous single-channel on-chip suppression.[3,8] We tested first-generation AstroPIC photonic chips that featured an alternate fabrication method with improved feature size and demonstrated mesh suppression functionality across both versions of the chip for normal-incidence grating couplers with 81% to 85% coupling.[4,9]

2 Photonic Integrated Coronagraph

2.1 Linear-Operator Formulation and Assumptions

Any optical system (with conventional components such as mirrors, lenses, and masks) that has an input plane and an output plane is mathematically equivalent to a linear passive operator transforming the electric field at the input plane into another electric field in the output plane.[10,11] An optimal linear operator for the coronagraph can be computed (which removes specific low-order modes from input to the output plane), with theoretical science yields several times greater than for bulk-optic coronagraphs designed to date. These are largely independent of aperture obstructions, segmentations, or struts and can significantly relax sensitivities to aberrations.

The assumptions used in this formulation are that the coronagraph can be modeled as a passive linear operator and that the complex electric field amplitudes have a finite-dimensional representation. Unless otherwise noted, numerical calculations in this overview utilize a single polarization state and a wavelength- and polarization-specific photonic coronagraph operator (with polarizations and broadband supported by parallel meshes) with throughput losses accounted for separately in the yield and experimental sections. The finite number of photonic spatial channels corresponds to a discretization of the pupil and therefore limits the spatial frequencies and field of view that can be represented by a specific mesh.

2.2 Photonic Coronagraph Implementation with MZI Meshes

The desired coronagraphic transformation is implemented by a programmable mesh of Mach–Zehnder interferometers (MZIs) on a photonic chip, originally developed for telecommunication applications such as wavelength multiplexing, optical switching and modulation, optical neural networks, and quantum information processing. The mesh sorts the input stellar electric field into one or more rejected output modes while preserving off-axis planet light in transmitted modes. This mode-sorting interpretation is central to the architecture, enabling both high-order starlight suppression and the ability to reconfigure the coronagraphic order to optimize the mesh for different targets and aberration states. The reconfigurability of the mesh through the programmable phase shifters provides additional degrees of freedom not available in fixed classical coronagraph masks.

The significance of a photonic coronagraph for HWO is driven by the paradigm shift enabled by PICs, in particular, the fact that a forward mesh of MZIs with tracked phase delays can implement a universal linear operation[12] and thus implement the functionality of any conceivable optical system (e.g., a theoretically optimal coronagraph[11]), at least in the limit of a large number of modes.

Thus, PICs provide a practical means to implement near-optimal coronagraphy, providing key advantages via a compact footprint. This has the potential to improve both science and cost margins and reduce technical risk to science yields. This is made possible by an architecture with improved alignment and stability tolerances over bulk-optic components and reduced sensitivity to upstream wavefront aberrations, eliminating the need for a separate deformable mirror for wavefront control via programmability and mode-sorting on-chip. Perhaps most importantly, by improving the efficiency and effectiveness of the overall observatory, a photonic coronagraph instrument increases the yield of exoplanet discoveries and enables more relaxed aperture requirements, accommodating wider struts, larger segment gaps, larger secondary obstructions, and less stringent stability requirements. The photonic coronagraphic mesh can also be dynamically reconfigured for individual observations to select an appropriate trade-off between tolerance to low-order modes and inner working angle (IWA).

The baseline concept for the AstroPIC photonic integrated coronagraph for HWO is shown in Fig. 1 with a 16-mode spatial representation (that can be scaled up to additional modes). It comprises (1) a lenslet array that samples the telescope pupil (or, alternatively the image plane, or any other plane) and focuses light into an array of grating couplers, (2) grating couplers that inject an orthogonal set of PIC input modes, (3) an MZI mesh that transforms the input modes into an output basis to optimally separate signal (planet/disk) from starlight, and (4) on-chip photodetectors (or, alternatively, off-chip detectors fed by fibers). By programming the mesh, the detector array can realize an image plane, a Lyot plane, or any other convenient output plane. If planet locations are known, individual output modes can be tuned such that all the planet light goes to a single-output channel (a kind of optical deconvolution of the planetary point spread

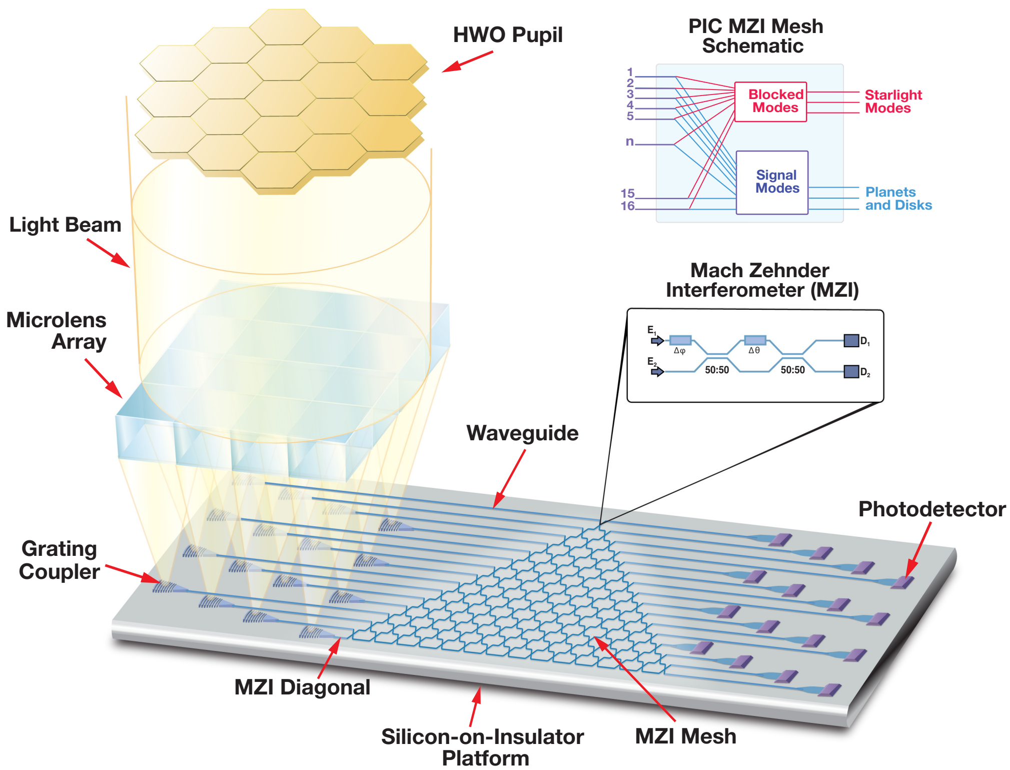

Fig. 1 Illustration of AstroPIC photonic integrated coronagraph concept for HWO shown here with 16 input channels and output channels, though we envision scaling up to higher numbers. A free-space optical beam from the telescope pupil is coupled using a microlens array onto a PIC device. At the focus of each lenslet is a grating coupler that feeds that portion of the input beam onto an individual waveguide, and represents a single-input channel. Each input channel represents a mode or basis vector in an orthogonal basis (16-dimensional, in this example), and the coupling operation projects the input beam onto that basis. Each input mode/waveguide contains a mix of noise (starlight) and signal (planet and disk light). The MZI mesh (here shown with four diagonals) transforms the input basis into an output basis where the starlight is maximally concentrated in as few output modes as possible. The remaining output modes contain mostly light from planets and disks. The intensities of output modes are captured by on-chip photodetectors (as shown) or coupled out to an external detector and can be configured to contain maximal light from each planet (or represent samples on an image or Lyot plane). The actual mesh uses equal path lengths to maintain coherence at each MZI.

function or PSF). This way, the planet signal is not limited to the PSF core, and the wings of the planet PSF contribute to the signal, without increasing noise.

We configure the MZI mesh by tuning the two phase shifters in each interferometer (see zoom-in detail in Fig. 1). Actuation can be via thermo-optic heaters (currently implemented in our prototype device), micro-electromechanical system devices (MEMS), or electro-optic components. In the limit of perfect phase shifters, lossless couplings, and ideal waveguide transmission with no back-reflection, each interferometer implements a tunable beam splitter (a simple rotation matrix combining the two input electric fields with a controllable ratio). Operation of the photonic coronagraph would first preset a priori the MZI phase settings (by voltage calibrations) to one corresponding to one of the "optimal coronagraphs." The coronagraph's contrast, IWA, and throughput are determined by the number of starlight modes "blocked," which defines the coronagraph order. These modes can also be used for a low-order wavefront sensor.

This initial configuration is equivalent to creating a static coronagraph prior to wavefront control. The photonic coronagraph can then be adjusted by running an inverse-propagation algorithm[12] to fine-tune the coronagraph into an energy-sorting configuration with minimal changes in the phase settings from their initial configuration and account for departures from the calibrated settings. This fine-tuning is equivalent to wavefront control using a deformable mirror in a traditional coronagraph.

2.3 Coupling Architecture and Photonic Chip Interface

The AstroPIC architecture utilizes a mapping between the continuous free-space HWO telescope pupil and the finite set of input waveguide channels at each of the grating couplers on the photonic chip. In the current demonstrations, this is accomplished using free-space relay optics combined with a microlens array that maps subapertures of the pupil onto an array of grating couplers. Each grating coupler feeds one waveguide channel of the MZI mesh, converting the incident pupil field into a finite set of complex modal amplitudes processed on chip.

The microlens array approach is baselined because it provides a compact, high-fill-factor mapping between the pupil and the grating-coupler array, similar to that used successfully for charge-coupled device camera chips. However, the photonic chip mesh can also be coupled via alternative approaches depending on the overall instrument requirements. These include direct optical-fiber injection for component-level testing of the chip, free-space relay optics without a microlens array for simplified demonstrations, and free-space coupling via photonic-lantern (that could include some level of modal remapping) with individual fibers feeding to the chip via either edge-couplers or grating couplers. The photonic chip interface used for the demonstrations in this paper supports the baseline architecture described earlier, with details including specific fabrication runs and packaged chips described in Sec. 4.

2.4 Architectural Limits

We outline here several limitations that follow from the finite-dimensional photonic implementation and represent limits compared with the theoretical performance possible with an optimal coronagraph. First, the finite number of spatial channels limits the highest spatial frequencies represented by the mesh, which appears primarily as an outer-working-angle limit and as throughput roll-off at larger angular separations. Second, current grating couplers introduce throughput losses and finite spectral bandpass, making coupling efficiency one of the dominant drivers of end-to-end performance, especially in terms of throughput. Third, present demonstrations are using silicon photonic substrates, which leverage telecom component developments around 1550 nm (C-band) in near infrared but may require additional substrates such as silicon nitride to cover the entire near-infrared down to 0.9 to 1 μm. Last, the ideal optimal coronagraph used in the architecture model must be realized by fabricated MZI cells that feature directional-coupler splitting-ratio errors, phase-calibration errors, thermal crosstalk, and path-dependent insertion loss with manufacturing tolerances starting to be exposed through dedicated fabrication runs.

2.5 Path Forward

The architectural development path is therefore focused on increasing the number of usable spatial channels, which represents a scale-up in mesh complexity, exploring sparsity and degrees of freedom required for the mesh architecture, improving both coupling efficiency and bandwidth of free-space coupling components such as the grating couplers, and utilizing architectural redundancy to compensate for component-level imperfections. Future AstroPIC tape-outs will test higher-throughput coupling structures, larger pupil-sampling meshes, achromatized directional couplers and phase shifters, and mitigation options to reduce both optical and thermal cross-talk. In parallel, the simulation pipeline described in Sec. 3 will be extended to include measured component nonidealities to improve fidelity to fabrication-informed performance estimates.

3 Yield Studies for HWO

3.1 Yield-Modeling Assumptions and Context

We have developed a simulation pipeline[7] used to predict the science yield of different configurations of the AstroPIC coronagraph for HWO, and enable photonic coronagraph architecture trades. This simulation framework can help identify areas of greatest impact for additional technology development and maturation. In addition, the simulation pipeline can validate predicted performance against experimental results and optimize the coronagraphic mesh configuration under different conditions, including increasing bandwidth by utilizing additional degrees of freedom and wavefront control of both static and time-varying aberrations. The concept of operations adopted for this study is that of a stand-alone near-infrared coronagraph that performs both imaging and discovery to enable comparison with the baselined coronagraph; the architecture is not NIR-limited, however, and with appropriate choice of substrate (e.g., silicon nitride) and design, can be adopted for the visible band.

For clarity, the coronagraph design survey (CDS) is the simulation pipeline used here to represent coronagraph performance in a form compatible with exoplanet yield calculations and evaluate via design reference mission simulations. The exploratory analytic concepts (EACs) are representative HWO telescope-aperture geometries used for architecture trades; in this paper, EAC-1 and EAC-2 denote off-axis hexagonally segmented and keystone-segmented apertures, respectively, whereas EAC-3 denotes an on-axis keystone-segmented aperture featuring both secondary obscuration and support struts. Telescope pupil sensitivities have been performed as part of a representative HWO coronagraph and yield studies[5] to compare aperture concepts and coronagraph architectures across the HWO program. FRIDAY refers to the remote server used to interface with the AYO design reference tool[13] used for the HWO trade studies in which the photonic coronagraph operators were evaluated.

3.2 Numerical Modeling and Yield-Modeling Pipeline

The numerical pipeline consists of several modules that connect the telescope–pupil electric field, the finite-dimensional photonic coronagraph operator, and the mission-level yield calculation. First, a free-space coupling module enables representation of the propagation of electric field from the telescope pupil (including potentially any upstream optics of the coronagraph such as the optical telescope assembly or deformable mirrors, if present), through the microlens array to complex-valued electric field amplitudes that sample the full-telescope pupil at the grating couplers and represent the input to the MZI mesh by computing the overlap integral. Second, the programmable MZI mesh itself implements an arbitrary unitary matrix operation, transforming the input channels to output channels in a fully universal way. Idealized propagation through a full upper triangular Reck mesh[14] enables decomposition of any unitary matrix through the MZI mesh (with the Reck layout using symmetrical, balanced paths through additional path length structures added for phase matching along each path). The layout and energy-sorting functionality is compatible with a more compact Clements mesh[15] or a series of binary trees.

On the back end of the mesh, we convert the photonic output to an equivalent Lyot-plane representation for compatibility with the simulation framework.[5] Although the MZI mesh can in principle be programmed to produce an image-plane-like output or an optical deconvolution of planetary point spread functions, the yield tools used here treat coronagraphs as pupil-to-pupil optical systems. The equivalent Lyot-plane interface, therefore, allows the PIC operator to be evaluated within the same simulation framework used for conventional coronagraph designs and then passed to design reference mission simulators such as AYO[13] and ExoSIMS.[16]

The yield calculations presented above assume a 20% bandwidth, consistent with current coronagraph designs. The photonic coronagraph's small mass and volume enable multiband layouts using spectral multiplexing. This can be done in one of three ways, sorted from lowest performing but most mature to highest performing but least mature: (1) split wavelengths off-chip (e.g., with dichroics) and handle different bands with separate small chips; (2) split wavelengths on-chip and handle different bands with separate MZI meshes on the same chip; and (3) use a more complex MZI mesh with additional degrees of freedom to enable full chromatic control of a large band. Simulations show that a full-triangular mesh is already sufficient to enable 2.5% sub-bands, with only three to four diagonals needed to reach monochromatic high-contrast performance.[7] Thus, 20% is not a physical limit; stacked or parallel meshes can extend bandwidth and enable simultaneous multichannel characterization. In companion simulations, a single MZI mesh achieved $\sim 10^{-10}$ contrast over the 2.5% bandwidth by optimizing additional degrees of freedom beyond the monochromatic case. Tiling a 20% band with ∼8, such 2.5% sub-bands would therefore require only a practical number of meshes and MZI meshes, keeping device scale feasible. Furthermore, additional optimization could extend the bandwidth on a single mesh beyond 2.5%.

3.3 Contrast and Throughput Evaluation of Finite-Channel PIC Operators

A range of photonic coronagraph operators was generated and evaluated using this simulation framework. Previously, these included a low-count 16-channel architecture and a 400-channel full photonic chip AstroPIC[17] evaluated for both order 4 and order 6 starlight suppression and for both the off-axis and on-axis pupils (corresponding to HWO EACs 1 and 3). In Fig. 2, the plotted contrast is computed as $C(\theta) = I_*(\theta)/I_{p,\mathrm{peak}}(\theta)$, the residual stellar intensity normalized by the local off-axis planet PSF peak throughput at the same angular separation θ. Thus, each image pixel is divided by the local exoplanet's PSF peak throughput, so the contrast is reported relative to the detectability of a companion at that separation. For the finite-star case, the stellar intensity is the average of 50 point-source images sampled across a stellar disk of diameter $0.05\lambda_0/D$. Total aperture throughput is defined as the fraction of light from an off-axis point source (injected as a pupil phase ramp) that remains after propagation through the coronagraph system. The input pupil field is normalized to unit incident power, so that throughput is summed output-plane intensity weighted by output sampling.

We show the aperture throughput and radial contrast curves for a finite source for a variety of AstroPIC designs. These include PIC operators for both on-axis and off-axis HWO aperture, with different numbers of channels, including the 16 and 400 channels point designs discussed in the architecture section, and also both a fourth-order and sixth-order starlight suppression. Also shown are optimal coronagraph operators at both order 4 and order 6 using the off-axis HWO aperture as a bounding case, with the optimal order 4 closely matching the IWA (star-planet separation corresponding to half the maximum aperture throughput) of the corresponding order PIC and similarly for the order 6. MZI meshes implementing photonic nulling for coronagraphs of orders 4 and 6 correspond to increasing numbers of sorted energy modes being blocked.

The total aperture throughput curves demonstrate nulling and show the inner working angle for different order PIC coronagraphs. These are well matched with expectations from optimal coronagraphs,[11] which set a performance bound on both inner working angle and maximum throughput achievable. The primary limitation from a finite number of modes arises in terms of the achievable outer-working angle. The finite number of modes is responsible for the throughput rollover loss at increasing angular separations and would require additional modes across the PIC to enable a larger field of view for detection and characterization. At a small enough number of modes as illustrated in the 16-channel curves, the maximum achievable aperture and inner working throughput are not reached before the outer-working angle roll-off occurs. Higher-order coronagraphs are naturally more robust to finite stellar diameter, but just as with traditional coronagraphs, this comes at the expense of inner working angle (IWA) as well as throughput close to the IWA. However, PICs can achieve the optimal combination of IWA and stellar diameter robustness that is unattainable by many traditional coronagraph architectures.

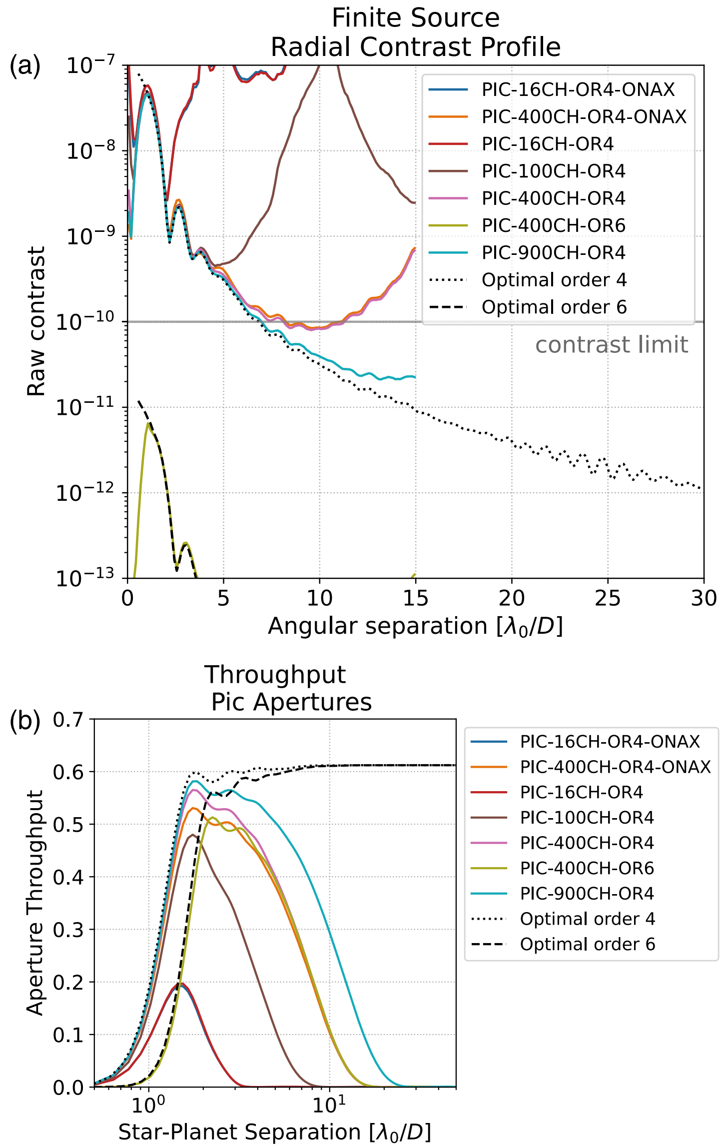

Fig. 2 Contrast and throughput curves for different AstroPIC point designs with varying numbers of channels, starlight suppression order for both off-axis and on-axis HWO apertures, and comparison with the optimal coronagraph boundary. (a) Contrast curves for the finite star of $0.05\lambda/D$ diameter star at 20% bandwidth. (b) Corresponding throughput curves as a function of angular separation.

The radial contrast curves as a function of angular separation for a finite diameter source also illustrate the improvement in robustness for a higher-order coronagraph and performance improvements possible with higher numbers of modes. The finite star used here has a diameter of $0.05\lambda/D$ (without applying limb darkening), i.e., more than 80% of the current HWO target list would be inside this stellar diameter.[18] Meanwhile, point sources are optimally suppressed by the PIC coronagraph. The sixth-order PIC operator shows excellent robustness to stellar diameter, whereas the fourth-order PIC operators, as described in the yield results in the previous section generate high yields, and their small inner working angles and high throughput make them excellent at characterizing smaller diameter stars.

3.4 Yield Sensitivity to Aperture Geometry, Spatial Channels, and Throughput Loss

The simulation pipeline also allows performing parametric sweeps of different telescope apertures, aberrations, and photonic coronagraph operators to determine yield sensitivities. In each

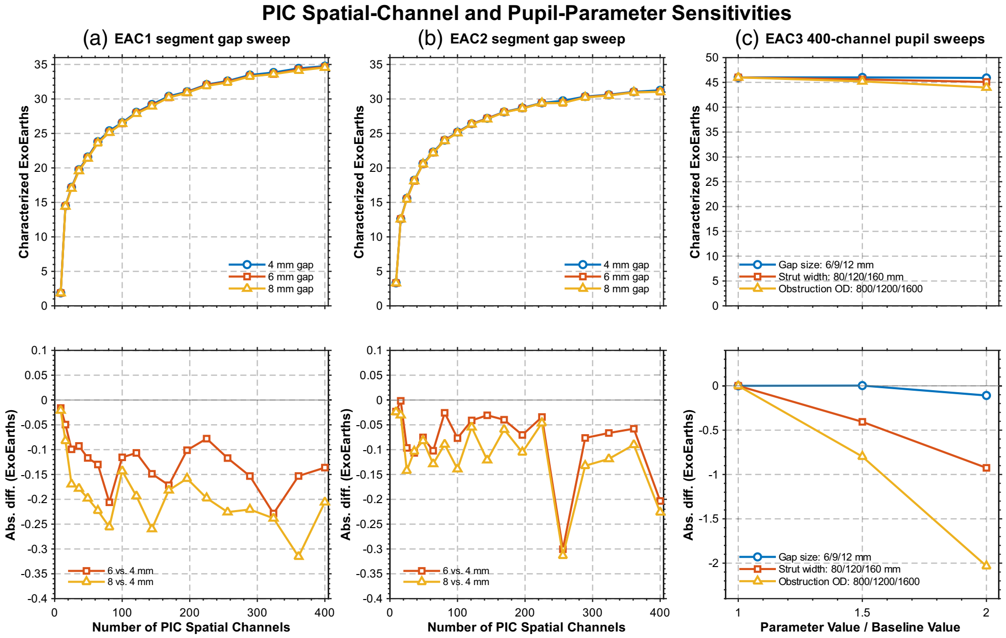

Fig. 3 Integrated photonic coronagraph robustness of characterized exo-Earth yield as a function of spatial-channel count and pupil-feature size for three HWO exploratory analytic concepts. The figure is arranged as a 2 by 3 panel layout: panel (a) shows the absolute characterized exo-Earth yield, and panel (b) shows the absolute yield difference relative to the nominal pupil-feature case. (Left column) EAC-1: off-axis, hexagonally segmented; segment-gap scale varied over 4, 6, and 8 mm, with differences referenced to the 4 mm nominal gap case. (Middle column) EAC-2: off-axis, keystone segmented; segment-gap scale varied over 4, 6, and 8 mm, with differences referenced to the 4 mm nominal gap case. (Right column) EAC-3: on-axis, keystone-segmented with secondary obscuration and support struts; 400-channel sweeps are shown for strut widths of 80, 120, and 160 mm, segment gaps of 6, 9, and 12 mm, and central-obscuration diameters (ODs) of 800, 1200, and 1600 mm. For EAC-3, the horizontal axis denotes each pupil-feature value normalized by its nominal first-listed value, and yield differences are referenced to the corresponding nominal feature dimension.

case, a new photonic coronagraph is configured to account for the updated telescope pupil and corresponding yield simulations performed. In recent HWO trade studies, we evaluated the robustness of PIC-based coronagraphs by measuring the characterized exo-Earth yield under 1 to 2× pupil-feature oversizing across three EACs, as shown in Fig. 3. For EAC-3 (on-axis, keystone-segmented with a secondary and struts), we swept strut widths of 80, 120, and 160 mm; segment gaps of 6, 9, and 12 mm; and central-obscuration diameters of 800, 1200, and 1600 mm. For EAC-1 and EAC-2 (off-axis hexagonal/keystone), we varied segment gaps of 4, 6, and 8 mm. Across all cases, PIC designs were nearly insensitive to feature-size changes; the small yield impacts observed are driven primarily by reducing the aperture collecting area through obscurations and segmentations.

Using our mesh simulation pipeline, we can probe yield sensitivities via parameter sweeps of the photonic coronagraph itself. For EAC-3 operators with typical assumptions for EAC-3 incorporated into FRIDAY scenarios, Fig. 4 shows (left) characterized exo-Earths versus the number of PIC spatial channels sampling the pupil and (right) characterized exo-Earths versus parametrized end-to-end throughput loss. Although absolute yields depend on mission assumptions, the trends are robust: ∼25 channels can help meet the HWO baseline goal (25 exo-Earths) for the EAC-3 aperture and ∼100 channels recover ∼80% of the asymptotic yield. Similarly, for throughput sweeps: ≥40% end-to-end transmission is required to reach the baseline goal, and ≳30% already recovers substantial science performance. These values were computed assuming ideal PICs sweeping one parameter at a time, so the real science yields would be somewhat lower. However, these simulations show the surprising result that scaling to thousands of channels is not strictly necessary to achieve HWO science.

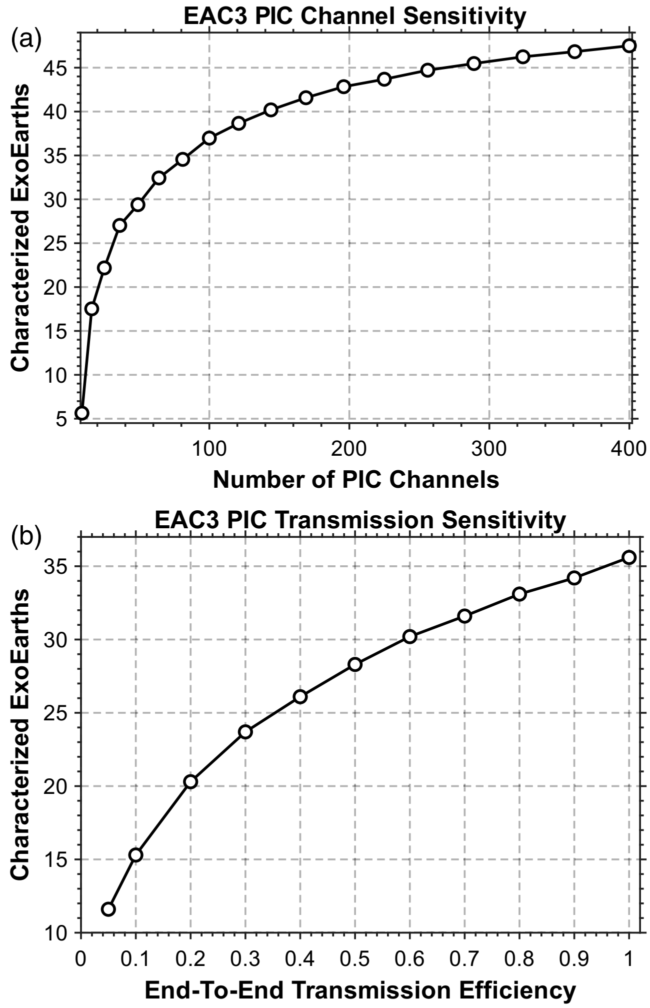

Fig. 4 Yield sensitivity of the photonic coronagraph to key parameters for HWO EAC-3. (a) Number of characterized exo-Earths versus pupil-sampling spatial modes. (b) Number of characterized exo-Earths versus end-to-end transmission efficiency.

3.5 Robustness to Upstream Wavefront Aberrations

For EAC-1 with a 400-channel photonic coronagraph, we sweep global Zernike amplitudes Z_2–escaped;Z_8 from 10^{-4} to 1–2 waves rms to explore exoearth candidate yield behavior in the presence of static aberrations applied at the telescope pupil, as shown in Fig. 5. With a fourth-order setting, the coronagraph blocks tip and tilt while passing higher orders; moving to a sixth-order setting also rejects defocus and astigmatism; an eighth-order setting further blocks coma and trefoil at some cost in characterized yield. Selecting the coronagraph order per target makes effective use of the PIC's reconfigurability and maximizes yield in the presence of these static aberrations. Although only static aberrations are evaluated here, the same reconfigurable strategy can be applied in the future to dynamic aberrations and can be combined with wavefront control to further improve performance.

Two practical paths emerge : (1) A hybrid approach uses a modest PIC (about 16 to 36 spatial modes) either in series or in parallel with a traditional coronagraph. For the parallel option, a pick-off is used inside the traditional coronagraph's IWA, providing additional science signal and optionally serving as a configurable low-order wavefront sensor[19] with near-term manufacturability. For the serial hybrid approach, a PIC either in a pupil or focal plane after the traditional coronagraph[20] would benefit from a relaxation in contrast (by several orders of magnitude requiring only 1×10^{-2}) to 1×10^{-3} (at the cost of serial throughput losses) by placing the photonic coronagraph as a second stage following a traditional coronagraph,[20] and (2) a full-photonic chip with hundreds of channels (e.g., 400) operates as a stand-alone coronagraph, with reconfigurable

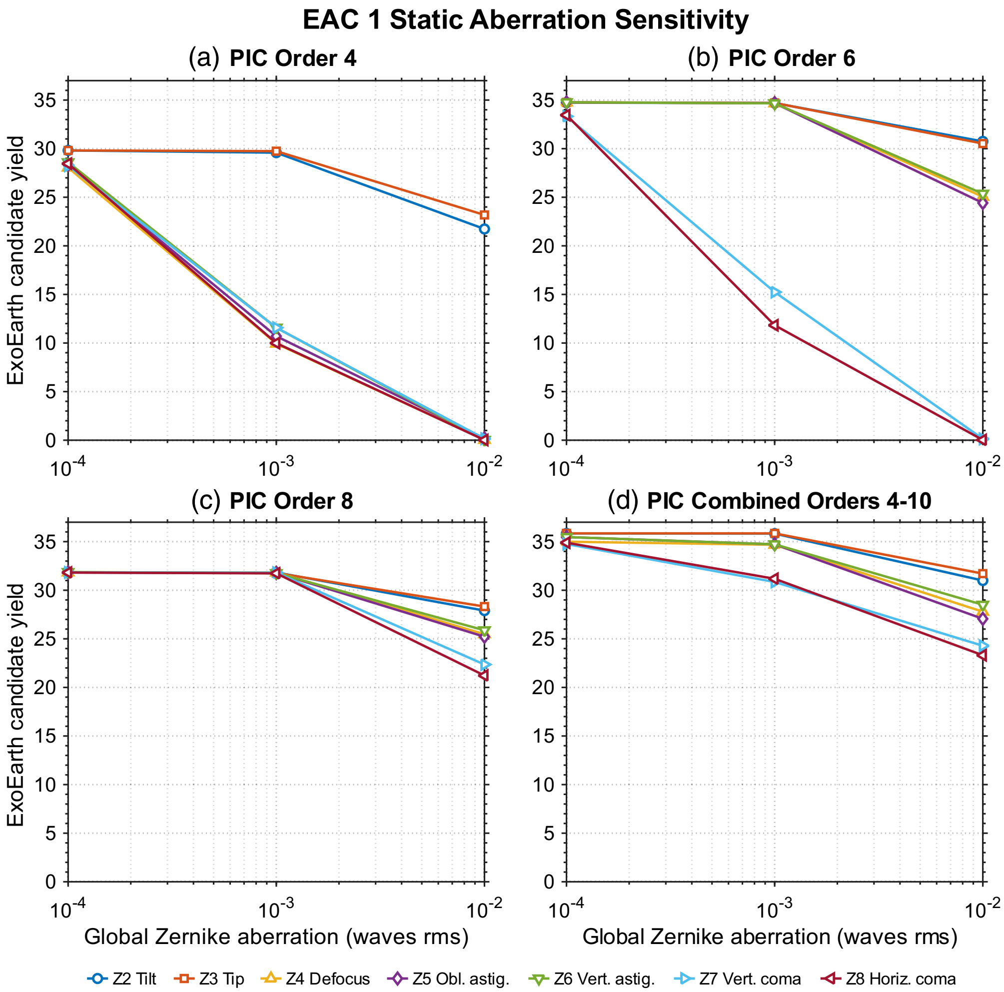

Fig. 5 Yield sensitivity of a photonic coronagraph to global Zernike aberrations Z_2–escaped;Z_8 applied to the EAC-1 pupil over 10^{-4} to 10^{-2} waves rms. (a) Order 4 is robust to Z_2–escaped;Z_3 (tip/tilt). (b) Order 6 is robust to Z_2–escaped;Z_6 (adds defocus, astigmatism). (c) Order 8 adds robustness to Z_7–escaped;Z_8 (coma, trefoil) with some yield cost. (d) Per-target order optimization maximizes characterized exo-Earth yield and improves robustness to static aberrations.

modes that offer the greatest science return, but it requires further maturation in contrast, throughput, bandwidth, and robustness before flight. Alternatively, the full-photonic coronagraph instrument can be deployed during servicing, which HWO will be built to support.

3.6 Manufacturing Tolerances, Nonideal Photonic Components, and Yield-Modeling Path

The robustness studies above address perturbations applied to the telescope pupil and upstream optical wavefront. For a manufactured photonic coronagraph, an equally important question is how closely the fabricated chip realizes the intended mesh operator. For the purposes of these yield calculations shown here, each MZI element is assumed to act as intended. In practice, the realized transformation is affected by component-level nonidealities such as directional-coupler splitting-ratio errors, residual phase offsets, finite heater resolution, voltage-to-phase-calibration drift, thermal crosstalk between heaters, and other effects, which can be incorporated into the same simulation pipeline by replacing ideal MZIs with parameterized nonideal transfer matrices. The resulting mesh operator can be evaluated with the same metrics used for the ideal operators (contrast, off-axis throughput, inner and outer-working angle, and exo-Earth yield). In addition, the mesh can be re-programmed in a similar way to wavefront control using a DM in the presence of aberrations on a bulk-optic coronagraph to correct for component nonidealities.

The next step for yield modeling is to combine ideal-operator studies shown here with fabrication-informed tolerance models and experimentally measured component properties. This approach will allow future yield studies to move toward statistically meaningful yield predictions with uncertainty bounds tied to measured chip performance and allow the simulation pipeline to fully support the technology-maturation roadmap described in Sec. 5.

4 Experiments

4.1 Experimental Scope and Testbed Measurement Physics

This section summarizes recent experimental progress and presents a unified status update for the AstroPIC program. The experiments establish system- and component-level readiness across both the Stanford photonics testbed and the newly commissioned photonics testbed at NASA Ames. Together, these test stations validate the Ames photonics testbed, demonstrate deeper on-chip photonic nulling than in previous single-input/single-output experiments, demonstrate multi-input operation using a free-space coupling module, and validate recently manufactured commercial chips that have been packaged, wirebonded, and precisely aligned with fiber-array units.

The primary experimental quantities reported here are stellar suppression or contrast, off-axis throughput where measured, coupling efficiency, and bandpass. As these demonstrations differ in configuration, these quantities should not be interpreted as simultaneous end-to-end flight performance values.

Figure 6 shows the implementation of the Ames photonic coronagraph testbed. The experimental quantities reported throughout this section, tabulated in Table 1, follow from these three types of measurements. For a single-input nulling measurement, the measured suppression or extinction is reported as the intensity in the output channel after nulling in a single-channel output compared with the total stellar energy summed across all output channels. For free-space coupling, a beam compressor remaps a fiducial telescope pupil to the grating-coupler array on the chip, illuminating all grating couplers; a microlens array enables a high-fill factor and improvements in signal-to-noise ratio. Coronagraphic throughput can be measured as the source is moved off-axis to simulate an exoplanet signal.

4.2 Photonics Testbeds

The AstroPIC project supported the build-up of two photonics test stations at Ames and Stanford. The Ames photonics testbed is shown in Fig. 6. The testbed status and recent experimental results are described in detail in a related paper[3] and are oriented toward system-level demonstrations and deep-contrast performance with realistic HWO-like pupils. The testbed at Stanford is focused on component-level development and testing. The Ames photonic testbed targets 1×10^{-9} contrast for a single-input channel and 1×10^{-7} contrast with an HWO-like pupil. The setup supports free-space and fiber coupling on/off-chip, programmable phase shifters across the MZI mesh, and readout from on-chip photodetectors, enabling measurement of 1×10^{-10} contrast. Other features include PIC thermal control and top-view IR plus side-view visible microscopy for alignment and diagnostics. The Stanford testbed[8] emphasizes novel functionality and component validation. The Ames testbed was commissioned in the summer of 2025 and has since been used to demonstrate greater than $1 \times 10^{-9}/90$ dB contrast for a single-input channel and a functional demonstration of multiple illuminated inputs using a free-space coupling module.

The roadmap to higher contrast with an HWO-like pupil follows an experimental fidelity progression. First, single-input and single-output measurements establish the intrinsic mesh suppression floor, chip stability, and manufactured chip realization. A second stage of fidelity uses simultaneous illumination of the full-input grating array with the microlens array and thus validates multichannel operation and coronagraphic functionality (on-axis suppression versus off-axis signal pass through). Third, closed-loop optimization of all phase shifters is used to optimize the stellar null for an HWO-like segmented pupil. Finally, the photonic coronagraph can be tested in hybrid configurations downstream of a conventional coronagraph and/or deformable-mirror system to evaluate using the PIC either as a serial second stage or as a parallel low-order wavefront sensor with a science capability, prior to demonstrations in a relevant vacuum environment. This technology development roadmap is described in Sec. 5.

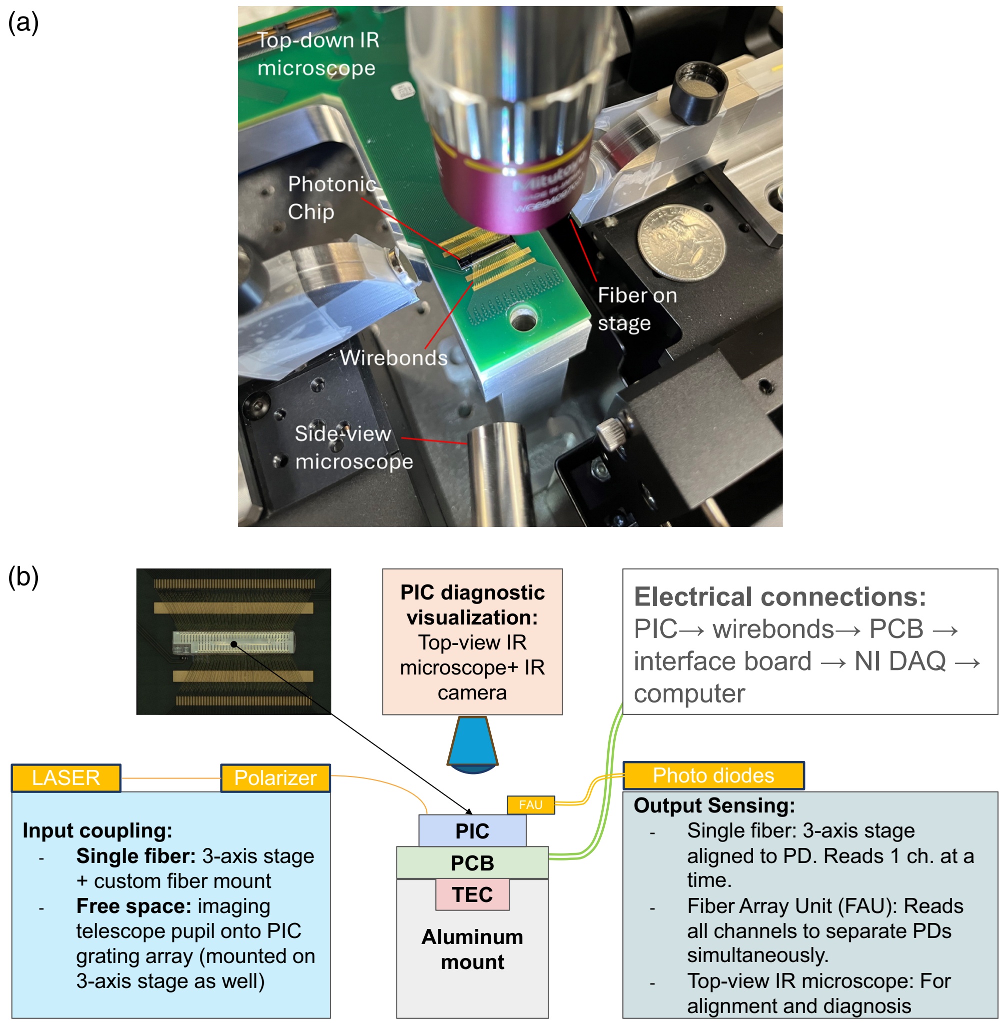

Fig. 6 (a) Photograph of photonic test station at the Ames coronagraph testbed showing the top-down IR and side-view optical microscope for alignment, the input and output fibers on alignment stages, and the photonic chip wirebonded to the printed circuit board. (b) Illustration of the key components of the photonics test station, including input and output modalities, electronic control of the chip, and diagnostic imaging.

4.3 Manufactured Chips

To date, AstroPIC photonic chips are fabricated as silicon photonic integrated circuits using commercial photonic foundry processes. This approach leverages manufacturing infrastructure developed for telecommunications, optical switching, programmable photonics, photonic neural networks, and related integrated-optics applications. The AstroPIC tape-outs include both coronagraphic MZI meshes and dedicated test structures that allow individual components to be characterized before full high-contrast operation and enable adoption of validated components in subsequent tapeouts.

The Cycle-1 AstroPIC chip has been taped out and fabricated at two different commercial foundries that utilize different manufacturing methods.[21] Advanced Microfoundries (AMF) uses standard photolithography for multiproject wafer, leveraging the same foundry flow as the initial experiment demonstrated for AstroPIC that used an existing MZI mesh[8] that achieved 7.9×10^{-9} (81 dB) contrast in a single-input channel, minimizing output suppression. After fabrication of the dedicated Cycle-1 AstroPIC chip, a printed circuit board for the electrical interface to the chip was also commercially manufactured. The photonic chip has been commercially wirebonded by Silitronics Inc., as shown in Fig. 7(a), and most recently integrated with a fiber-aligned unit for simultaneous electronics readout. For scale, a handheld photonic integrated coronagraph display unit is shown, illustrating the miniaturization potential for astrophotonic-based instrumentation.

Table 1 Summary of AstroPIC experimental results to date, including stellar suppression, end-to-end or off-axis throughput, and bandpass where measured. The listed demonstrations emphasize different aspects of the technology-maturation path; suppression, throughput, and bandpass are not necessarily measured simultaneously in the same end-to-end configuration.

Experiment	Architecture / Config	Extinction (linear / dB)	Throughput	Bandpass	Active MZI Elems.	Ref.
Single-channel nulling, fiber in	4-MZI mesh (dual-config min/max)	1×10^{-7}/70 dB	Not measured	Monochromatic (1550 nm)	4	17
Single-channel nulling, fiber in	3-input triangular mesh with PMZIs along main path	7.9×10^{-9}/81 dB	Not measured	Monochromatic (1550 nm)	6	8
Single-channel nulling, fiber in	9-input triangular mesh (photolithography); single diagonal path controlled	2.0×10^{-9}/87 dB	9.5% end-to-end on-chip	Monochromatic (1550 nm)	8	3
Single-channel nulling, fiber in	9-input triangular mesh (e-beam lithography); single diagonal path controlled	6.3×10^{-10}/92 dB	8.7% end-to-end on-chip	Monochromatic (1550 nm)	8	3
Single-channel nulling, fiber in (deepest to date)	9-input triangular mesh (e-beam lithography); single diagonal path controlled	3.5×10^{-10}/94 dB	8.7% end-to-end on-chip	Monochromatic (1550 nm)	8	24
Free-space demo, no microlens	4-channel PIC; on-axis suppression and off-axis signal	1×10^{-4}/40 dB	Not measured	Monochromatic (1550 nm)	3	17
Free-space demo, microlens in (most channels to date)	9-channel PIC; on-axis suppression and off-axis signal	8.8×10^{-8}/71 dB	3.6% end-to-end on-chip, 41% off-axis planet	Monochromatic (1550 nm)	36	25
Free-space demo, microlens in (hybrid DM)	9-channel PIC downstream of DM	4×10^{-6}/54 dB	Not optimized	Monochromatic (1550 nm)	0	23
Component-level coupling demonstrations relevant to end-to-end throughput and bandpass:						
TWIG grating coupler	Normal-incidence inverse-designed grating couplers (component-level test structures)	N/A (component)	81% to 85% coupling efficiency	20 nm narrowband near 1550 nm	N/A	4

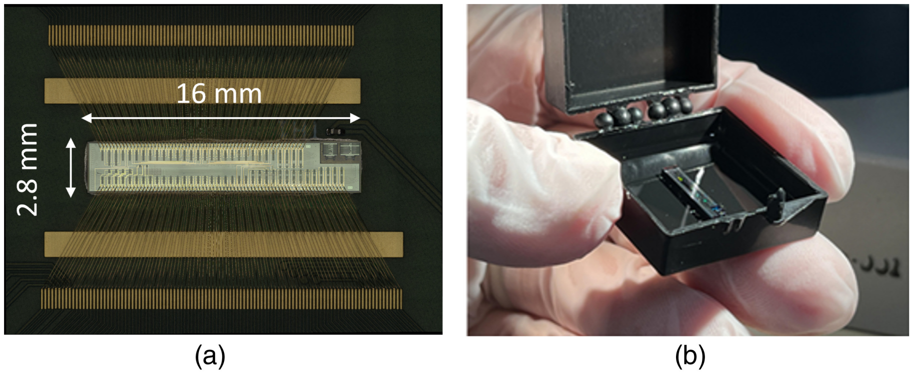

Fig. 7 Manufactured AstroPIC photonic chip with two independent coronagraphic MZI meshes and on-chip test structures. (a) Microscope image after wirebonding chip to host circuit board with chip dimensions indicated (courtesy of Silitronics Inc.). (b) Handheld photonic integrated coronagraph chip illustrating instrument miniaturization.

A similar layout was submitted to Applied Nanotools (ANT), which uses e-beam lithography, which has improved feature sizes and smaller-batch custom runs. This provides process flexibility for an additional etch step and allows the addition of a set of test structures to fabricate high-efficiency "three-wave interaction grating couplers" that were optimized via inverse design.[9] The photonic coronagraph device consists of a silicon-on-insulator PIC (2.8×16 mm reticle) with 1.55 um directional couplers and input/output grating couplers and integrates two coronagraphic meshes plus exploratory test structures. The first mesh is a triangular MZI mesh with nine-input modes and nine diagonals; a 3×3 input grating array supports free-space coupling via a microlens array, with bond-pad count setting phase-shifter and mode limits. This device enables higher-mode free-space experiments and measurements of throughput, inner/outer-working angles, and deep contrast. The second mesh is a seven-input, four-diagonal perfect-MZI mesh that doubles phase shifters per cell to reduce cross-channel leakage and target $\sim 10^{-9}$ contrast to enable correction of imperfect MZI performance.[22] Both meshes utilize standard grating foundries that limit end-to-end throughput. Additional test structures provide improvements in bandwidth and measurement of both polarizations.

Before using the MZI mesh for a high-contrast experiment, for a newly fabricated and packaged chip, the alignment of the input and output-fiber array to the on-chip grating couplers must be verified. Test structures are used to characterize propagation and insertion losses, the mesh routing and connectivity are verified by injecting light and mapping outputs, and the PIC must be brought to a stable operating point in temperature, wavelength, optical power, and input alignment. The output photodetectors should also be calibrated, and each phase shifter's voltage-to-phase response must be calibrated by sweeping voltage and fitting the MZI transmission. Finally, mesh-level calibration routines should be run to identify and load an initial bar-state setting of the mesh.

4.4 High-Contrast and Multi-input Demonstrations

The photonic chip can be operated either as a stand-alone or full photonic coronagraph or in combination with a bulk-optics coronagraph system, including a deformable mirror. For the experiments described in this section, the photonic chip is used for component-level tests, illuminated by a single-mode fiber (single-channel input mode) or in system-level tests with a conjugate HWO-like pupil illuminating the grating array, with the option of aligning a microlens to improve the fill factor. These input coupling modalities are shown in the three panes in Fig. 8. The first suppression experiment at the Ames Photonics Testbed used the nine-input full upper triangular MZI mesh described above for the AMF chip operating across a single MZI diagonal.[3] In this experiment, input light is coupled using a single-mode fiber into a single grating coupler, and a fiber is coupled to an output grating coupler that uses the longest diagonal of the nine-mode triangular mesh. The MZIs along the top diagonal are configured to minimize the power measured from the output port. The input laser is monochromatic and set to 1.55 um. The total power across all output modes is measured at the beginning and end of each experiment and is used to

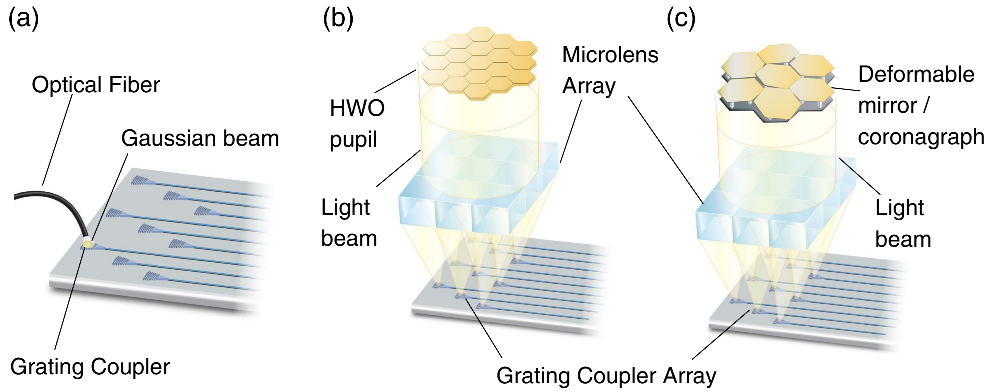

Fig. 8 Physical input modalities utilized for coupling into the photonic coronagraph. (a) Single-channel input for chip characterization, verification of mesh functionality, and validation of single-channel suppression; (b) higher-fidelity demonstration, which uses all input modes and couples (in free space) an HWO-like pupil into the chip; (c) another type of higher-fidelity demonstration where a deformable mirror serves as a stand-in for a telescope pupil (and can be coupled with a coronagraph) to emulate segment misalignments.[23]

compute the total contrast. The contrast measured at the end of this configuration process was 2.0×10^{-9} contrast (87 dB) with a measured throughput end-to-end on the chip of 9.5%. Repeating this procedure with a chip fabricated by ANT yielded an improved 3.5×10^{-10} contrast (94 dB), which is a factor of nearly 2 compared with the commissioning result of 6.3×10^{-10},[3] but with slightly worse end-to-end measured throughput on-chip of 8.7%. The suppression improvement on the e-beam lithography chip may not be due to the manufacturing method, but rather higher resolution of voltage input using the same interface board. The end-to-end measured throughput, for both chips, of ∼10% is similar to the previous prototype used,[17] and continued to be dominated by losses from standard, foundry-provided input and output grating coupler with ∼30% coupling efficiency; silicon waveguide propagation losses at 1.55 um are ∼1 dB/cm.

This suppression experiment demonstrated a factor of 10× improvement over the previous best suppression measured due to the usage of the dedicated Cycle-1 AstroPIC chip, which had additional MZI elements.[8] The significance of this result is that it demonstrates a deeper contrast level measured on-chip than previously, which is made possible by the additional MZI stages in the larger nine-channel mesh. In addition, it validates the measurement sensitivity of the testbed to levels approaching 1×10^{-10} contrast in-air. FAU-bonded units enabled improvements in stability, simultaneous read-out of multiple output channels, and integration with a free-space coupling module at the cost of reducing the end-to-end coupling efficiency on-chip to 3.6%.

Functional demonstrations are beginning to address system-level demonstrations with free-space coupling, which illuminates multiple input channels on the chip simultaneously with a fiducial pupil. The first free-space coupling demonstration utilized a single fiber backed-up vertically to illuminate four grating couplers simultaneously, which were configured to suppress on-axis light to 1×10^{-4} contrast, and passing signal through when offset laterally.[17] Most recently, free-space coupling demonstration of AstroPIC[24] with the nine-channel MZI mesh at Ames recently achieved 8.8×10^{-8} (71 dB)[25] on-axis coronagraphic suppression in a single-output channel with a free-space coupling module illuminating all nine-input gratings simultaneously while remapping a compressed pupil with a microlens array providing a high-fill factor, and measuring an off-axis planet throughput reaching 41% (fraction of incident planet light coupled into output dark channel), and utilizing all MZI elements available across the mesh. Second, a hybrid demonstration[23] used the AstroPIC chip free-space coupled with a microlens array downstream of the Santa Cruz Extreme AO Lab (SEAL) testbed's[26] at UC Santa Cruz and demonstrated 4×10^{-6} contrast (54 dB) in a single-output waveguide. In this case, the AstroPIC MZI mesh was unpowered, and thus, none of the MZI elements were actively controlled; instead, a Boston MEMS DM upstream of the PIC was utilized to perform nulling on the single-output waveguide with the goal of expanding this demonstration to operate downstream of a traditional coronagraph.[20]

4.5 High-Efficiency Three-Wave Interaction Grating (TWIG)

One of the primary performance drivers for a photonic integrated coronagraph is the end-to-end coupling throughput. Previous experimental demonstrations have consistently shown that standard foundry grating couplers with ≈30% efficiency dominate optical losses when coupling light on and off chip.[3,27] These gratings are optimized for oblique incidence near 1.55 um, which complicates instrument-level optical design. To address this limitation, the AstroPIC technology program has identified the development of high-efficiency, normal-incidence free-space grating couplers as one of the key directions for component-level optimization and demonstration.

Normal-incidence grating couplers are traditionally limited to ∼50% efficiency in silicon photonics due to material symmetry constraints. This limitation is overcome in the AstroPIC "three-wave interaction grating" (TWIG) designs by leveraging finer feature sizes enabled by electron-beam lithography and by suppressing back-scattering through engineered destructive interference. Designs optimized using adjoint methods achieved simulated peak coupling efficiencies exceeding 90% with tunable bandwidths.[9] Fabricated devices demonstrated up to 85% measured coupling efficiency with close agreement between simulation and experiment[4] providing a path for substantial improvements in throughput once these test structures are integrated into the coronagraphic mesh in a future device.

5 Technology Development Status

State-of-the-art demonstrations of photonic integrated circuits in the laboratory have advanced rapidly over the past several years to levels of programmatic interest to HWO. However, at present, these demonstrations are best classified as initial system-level results. They include high-efficiency on-chip coupling without coronagraphic functionality,[4,28] rapidly improving on-chip starlight suppression with a small number of spatial channels,[24] and industry-led demonstrations of large-format photonic meshes with thousands of input channels but without coronagraphic operation. In the AstroPIC project, we have focused on achieving deep on-chip suppression with architectures and configurations directly relevant to HWO; these results are summarized in Table 1.

We outline a development roadmap from the current state of the art to the maturity required for the consideration of a near-infrared photonic coronagraph channel for HWO. The current technology readiness level for AstroPIC is TRL 3, established by component-level demonstrations and initial system-level functional demonstrations on Cycle-1 chips. Subsequent maturation will proceed through TRL 4 component- and subsystem-level demonstrations under representative conditions, and ultimately to a TRL 5 demonstration in a relevant environment. The end objective of this roadmap is to reach TRL 5 prior to the start of the HWO phase A formulation/Mission Critical Review phase through an integrated system-level demonstration in a relevant environment. This will enable the option for the inclusion of a near-infrared photonic coronagraph channel in HWO, leveraging the architecture's advantages in mass, volume, inner working angle (within the typical $3\lambda/D$ of conventional coronagraphs), and reconfigurability. Our near-term goal is to complete component- and subsystem-level demonstration (TRL 4) before HWO technology down selection. Recent advances in photonic spectrographs[29] and energy-resolving detectors[30] further motivate connecting a photonic coronagraph to a downstream spectrograph for exoplanet characterization.

5.1 Current Status (TRL 3)

The Ames photonic testbed initial results (see Table 1) reached contrast levels of 3.5×10^{-10} contrast for a single-input channel and 8.8×10^{-8} contrast with an HWO-relevant pupil illuminating all input channels simultaneously.[24] Single-input/single-output measurements establish the intrinsic mesh suppression floor and testbed stability and a component-level TRL 2 demonstration, whereas simultaneous illumination of the 3×3 input grating array through a beam compressor sampled by a microlens array validates multichannel operation and off-axis throughput. The free-space demonstrations utilizing mesh self-configuration[12,24]establish TRL 3 maturity for the AstroPIC photonic coronagraph.

5.2 Near-Term Maturation (TRL 4)

Reaching TRL 4 requires component- and subsystem-level demonstrations under conditions representative of operation in HWO. The assumed TRL 4 threshold is a system-level experiment achieving 1×10^{-9} contrast with end-to-end throughput of at least 30% and broadband operation of ≥2.5%, with a path to broader bandpasses through spectral multiplexing of narrowband meshes.[7] This requires achromatic component validation (directional couplers, grating couplers, and phase shifters), high-efficiency normal-incidence grating couplers,[4] integrated photodetectors or high-efficiency *in situ* readout, and scaling of the active mesh to a larger number of simultaneously controlled MZI elements, including usage of a model-based approach. Hybrid demonstrations downstream of a conventional coronagraph or deformable-mirror system will evaluate the use of the PIC as a second-stage nuller and low-order wavefront sensor; the initial demonstration at the UCSC SEAL testbed[23] represents the first hybrid application of an AstroPIC photonic coronagraph with a deformable mirror, with nulling performed by the upstream DM.

5.3 Relevant-Environment Demonstration (TRL 5)

A subsequent maturation step is to repeat the most important nulling and throughput measurements in a vacuum environment representative of flight conditions. This will test whether heater calibration, thermal crosstalk, electronic packaging, fiber and free-space alignment stability, outgassing, and coupling efficiency remain stable in the absence of convective heat transfer. These steps define the path toward a TRL 5 demonstration of the near-infrared photonic coronagraph channel. Because the final HWO milestone dates and technology-maturation plan remain programmatically defined, we describe the schedule here in milestone-relative terms. Our goal is to complete component optimization and integrated laboratory demonstrations before HWO technology down-selection activities, and to target TRL 5 prior to the phase A formulation period (currently planned to begin in 2030, subject to the final HWO schedule, available resources, and the specific TRL entrance criteria adopted for the mission). For an early mission concept review requiring a TRL 5 assessment of the photonic coronagraph, the critical-path items are maintaining TRL 4 performance with vacuum-compatible packaging, multi-input HWO-like free-space nulling, broadband compatibility through spectral multiplexing of narrowband meshes, and repeatable closed-loop operation in conditions relevant for HWO.

5.4 AstroPIC Technology Readiness Matrix

To consolidate the AstroPIC development status against likely HWO needs, Table 2 compares working estimates of HWO-relevant performance with idealized simulated performance from the AstroPIC pipeline (Sec. 3) and current laboratory demonstrations (Sec. 4 and Table 1). The threshold and baseline columns represent the AstroPIC team's current working assumptions rather than formal HWO requirements; final values will be set by the HWO program. The simulated column reports performance achievable with idealized PIC operators, providing an architecture-level upper bound that does not yet include fabrication nonidealities. The demonstrated column reflects measurements obtained on the Cycle-1 chip.

6 Conclusion

In this paper, we provided an overview of the continuing progress on technology development for the AstroPIC photonic coronagraph. In addition to the miniaturization potential of an astrophotonic coronagraph instrument, we have shown through the optimization and modeling pipeline the potential benefits in terms of exo-Earth science yields, reprogrammability of the PIC, and robustness to upstream wavefront aberration for the Habitable Worlds Observatory mission architecture. We have shown that a PIC-based photonic coronagraph is widely compatible with all EACs 1-3 considered to date by the HWO project and is robust to significant variations in all telescope pupil parameters. In addition, we have shown the benefits of reconfigurability in terms of tailoring the photonic coronagraph to specific target observations and static aberrations, showing significant improvements in robustness and yield in the presence of varying levels of aberrations. The same reprogrammability provides a natural pathway to use the photonic coronagraph as the active wavefront controller (instead of deformable mirrors). We have shown that improvements that are now within reach in both coronagraphic throughput and a modest number of channels can enable a hybrid coronagraph to operate at first light, and a scaled fully photonic coronagraph with hundreds of modes can be added to HWO, potentially during servicing, to

Table 2 AstroPIC technology readiness matrix comparing potential HWO-relevant performance requirements with current simulated and experimentally demonstrated performance. Threshold and baseline values represent current best estimates of HWO requirements by the AstroPIC team with final values to be set by the HWO program. Simulated values correspond to idealized PIC operators evaluated through the AstroPIC simulation pipeline. Demonstrated values correspond to laboratory measurements summarized in Table 1.

Key parameter	Likely needed performance (threshold)[a]	Likely needed performance (baseline)[b]	Simulated (idealized) performance[c]	Current demonstrated performance
1. Contrast	4×10^{-10}	1×10^{-10}	$<1 \times 10^{-10}$	3.5×10^{-10} (monochromatic, single-channel)[24]
2. End-to-end planet throughput	25%	50%	70 to 90% (depends on design)	~10% (standard foundry gratings in mesh)[24]
3. Inner working angle and sensitivity to stellar diameter	$<4\lambda/D$ $>0.05\lambda/D$	$<3\lambda/D$ $>0.1\lambda/D$	$1.5\lambda/D$ $0.1\lambda/D$ (depends on order)	$\sim 0.5\lambda/D$ $<0.01\lambda/D$[d]
4. Number of input/output spatial channels	16	100	16 to 400 (depending on design)	9 (current Cycle-1 chip)[24]
5. Number of on-chip actuators for wavefront control	256	10^4	16^2 to 400^2 (depends on design)	36 active MZIs[24]
6. Bandwidth	10%	20%	20%	Monochromatic
7. exo-Earth Candidate (EEC) yield	15 EECs	25 EECs	~25 to 50 EECs at 100 to 400 channels for HWO EAC-3	Not yet demonstrated end-to-end

[a]Threshold values are working estimate of the minimum performance likely required to meet HWO science goals; final requirements will be defined by the HWO program.
[b]Baseline values represent likely performance needed to achieve the HWO baseline yield goal of 25 characterized exo-Earths.
[c]Simulated values are computed using idealized PIC operators in the AstroPIC simulation pipeline; chip-fabrication nonidealities are not yet included, but fundamental physics limits are accounted for.
[d]The demonstrated λ/D values correspond to laboratory chip-level measurements; the inner working angle relevant for HWO is set jointly by the chip architecture and the upstream optical relay.

augment its coronagraphic capabilities and efficiency. Furthermore, a key simulation result shows that additional degrees of freedom on an MZI mesh can be utilized to improve coronagraphic functionality—for example, supporting 1×10^{-10} contrast in a 2.5% band on a single MZI mesh,[7] which enables the realization of broadband photonic coronagraphs with parallel meshes.

The AstroPIC photonic coronagraph has demonstrated 3.5×10^{-10} contrast (94 dB)[24] on the chip in monochromatic light, representing an improvement of a factor of 2x compared with previous results.[3] In addition, a component optimization effort has been designed, fabricated, and experimentally verified normal-incidence high-efficiency grating couplers with measured coupling efficiencies ranging from 81% to 85% and demonstrating excellent agreement with the expected design simulation.[4]

Furthermore, recent system-level demonstrations with a free-space coupling module have demonstrated the photonic coronagraph to TRL 3 with operation of the entire coronagraphic mesh[24] as well as hybridization with a DM[23] when all input channels are simultaneously illuminated. Furthermore, a photonic source that simulates both the star and the planet is planned to demonstrate nulling of the star and retrieval of the planet signal through the photonic coronagraph.[31]

Disclosures

The authors declare there are no financial interests, commercial affiliations, or other potential conflicts of interest that have influenced the objectivity of this research or the writing of this paper.

Code and Data Availability

NASA regulations govern the release of source code, including what can be released and how it is made available. The software developed for this study includes numerical tools for photonic coronagraphic modeling, including optical propagation simulations, coronagraphic masks, and visualization. Readers interested in obtaining copies of the optical propagation, pupil modeling, or visualization software, as well as associated simulation data products generated in this work, should contact the corresponding author.

Acknowledgments

This work was carried out at the NASA Ames Research Center and Stanford University's ECE Department. The AstroPIC project is supported through NASA STMD's Early Career Initiative (ECI) program and the HWO Technology Maturation Project Office (TMPO). Resources supporting this work were provided by the NASA High-End Computing (HEC) Program through the NASA Advanced Supercomputing (NAS) Division at Ames Research Center. Artistic illustrations were drawn by Cheryse Triano at NASA Ames. Any opinions, findings, and conclusions or recommendations expressed in this article are those of the authors and do not necessarily reflect the views of the National Aeronautics and Space Administration.

References

1. N. Jovanovic et al., "Astrophotonics roadmap: pathways to realizing multi-functional integrated astrophotonic instruments," *J. Phys. Photonics* **5**, 042501 (2023).
2. NASA Astrophysics Division, "Emerging technologies for astrophysics missions (etam) workshop," 2025, https://www.nasa.gov/emerging-technologies-for-astrophysics-missions-workshop/ (accessed 21 August 2025).
3. R. Morgan et al., "Testbed design and high-contrast demonstration with the AstroPIC integrated photonic coronagraph," *Proc. SPIE* **13627**, 1362726 (2025).
4. C. G. Valdez et al., "Three-wave interaction grating coupler with the sub-decibel insertion loss at normal incidence," *Optica* **13**(2), 180–187 (2026).
5. R. Belikov et al., "Coronagraph design survey for future exoplanet direct imaging space missions," *Proc. SPIE* **13092**, 169 (2024).
6. C. Stark et al., "The exoEarth yield landscape for future direct imaging space telescopes," *J. Astron. Telesc. Instrum. Syst.* **5**(2), 024009 (2019).
7. K. Fogarty et al., "Modeling and optimization pipeline for the AstroPIC coronagraph," *Proc. SPIE* **13627**, 1362782 (2025).
8. C. G. Valdez et al., "High-contrast nulling in photonic meshes through architectural redundancy," *Opt. Lett.* **50**(11), 3660–3663 (2025).
9. C. G. Valdez et al., "High-efficiency vertically emitting coupler facilitated by three wave interaction gratings," *Opt. Lett.* **49**(9), 2373–2376 (2024).
10. O. Guyon et al., "Theoretical limits on extrasolar terrestrial planet detection with coronagraphs," *Astrophys. J. Suppl. Ser.* **167**, 81–99 (2006).
11. R. Belikov et al., "Theoretical performance limits for coronagraphs on obstructed and unobstructed apertures: how much can current designs be improved?," *Proc. SPIE* **11823**, 118230W (2021).
12. D. A. B. Miller, "Self-configuring universal linear optical component," *Photonics Res.* **1**, 1 –15 (2013).
13. C. C. Stark et al., "Paths to robust exoplanet science yield margin for the Habitable Worlds Observatory," *J. Astron. Telesc. Instrum. Syst.* **10**(3), 034006 (2024).
14. M. Reck et al., "Experimental realization of any discrete unitary operator," *Phys. Rev. Lett.* **73**(1), 58–61 (1994).
15. W. R. Clements et al., "Optimal design for universal multiport interferometers," *Optica* **3**(12), 1460–1465 (2016).
16. D. Savransky et al., "Quantifying the impacts of schedulability on science yield of exoplanet imaging missions," *Proc. SPIE* **12680**, 126801K (2023).
17. D. Sirbu et al., "AstroPIC: near-infrared photonic integrated circuit coronagraph architecture for the habitable worlds observatory," *Proc. SPIE* **13092**, 130921T (2024).

18. E. Mamajek and K. Stapelfeldt, "NASA exoplanet exploration program (ExEP) mission star list for the Habitable Worlds Observatory," arXiv: 2402.12414 (2024).
19. J. Lin, "Choice of optical transformation for photonic circuit wavefront sensors," *Appl. Opt.* **65**, 4377–4383 (2026).
20. E. Por et al., "A hybrid coronagraphic approach using photonic integrated circuits and bulk optics coronagraphs," *Proc. SPIE* **13092**, 130921U (2024).
21. D. Sirbu et al., "AstroPIC II: overview of technology development for a near-infrared photonic integrated coronagraph for the Habitable Worlds Observatory," *Proc. SPIE* **13623**, 1362309 (2025).
22. D. A. B. Miller, "Perfect optics with imperfect components," *Optica* **2**, 747 (2015).
23. E. H. Por et al.Hybrid photonic coronagraphy: integration and testing on the seal testbed," in *Spirit of Lyot*, Vol. **6**, Pasadena, CA (2026).
24. R. Morgan et al., "High-contrast demonstrations with the AstroPIC integrated photonic coronagraph," *J. Astron. Telesc. Intrum. Syst.*, in review (2026).
25. R. Morgan et al., "Laboratory update for the astropic integrated photonic coronagraph," in *Spirit of Lyot, Oral Presentation*, Vol. **6** (2026).
26. R. Jensen-Clem et al., "The Santa Cruz Extreme AO Lab (SEAL): design and first light," *Proc. SPIE* **11823**, 118231D (2021).
27. R. Marchetti et al., "High-efficiency grating-couplers: demonstration of a new design strategy," *Sci. Rep.* **7**(1), 16670 (2017).
28. D. McKeithen, J. Jewell, and J. K. Wallace, "Hardware development towards the demonstration of an ideal photonic coronagraph," *Proc. SPIE* **13092**, 130925V (2024).
29. P. Gatkine et al., "Efficient ultra-broadband low-resolution astrophotonic spectrographs," *Opt. Express* **32**, 17689–17703 (2024).
30. S. Steiger et al., "Simulated performance of energy-resolving detectors towards exoplanet imaging with the Habitable Worlds Observatory," *Proc. SPIE* **13092**, 130921W (2024).
31. E. Bendek et al., "Photonic source for binary source simulations," in *245th Amer. Astron. Soc. Meet.* (2025).

Dan Sirbu is a research scientist in the Astrophysics Branch at NASA Ames since 2014 and is currently the PI of the AstroPIC project. He holds his PhD in mechanical and aerospace engineering from Princeton University and his BSc in electrical engineering from the University of Alberta. His research focuses on high-contrast exoplanet imaging, starlight suppression systems including photonic integrated coronagraphs, and wavefront control and estimation.

Ruslan Belikov received his BSE with high honors from Princeton in 1999 and his PhD from Stanford in 2005 (both in electrical engineering). He has been at NASA Ames since 2008, where he created the Ames Coronagraph Experiment laboratory and Exoplanet Technologies research group. He specializes in the development of high-contrast imaging technologies to detect exoplanets, especially life-bearing ones, and was the PI of a precursor project to AstroPIC, which advanced the photonic coronagraph from TRL0 to 2. He has authored or co-authored over 300 publications and holds two patents.

Eduardo Bendek is a scientist and engineer with eleven years at NASA Ames and JPL. He contributed to the Roman Space Telescope Coronagraph Instrument and led exoplanet detection technology laboratories at both centers. NASA awarded him the Exceptional Technology Achievement Medal in 2015. He has contributed to NASA's Exoplanet Exploration Program and authored over 150 publications and multiple patents. He holds his BS and MS degrees in mechanical engineering and his PhD in optical sciences.

Kevin Fogarty is an astrophysicist at the NASA Ames Research Center. Previously, he was the Troesh Prize postdoctoral fellow at the California Institute of Technology and received his PhD from Johns Hopkins University in 2017, studying star formation in galaxy clusters. His current research interests include high-contrast imaging, developing new instrumentation concepts for astronomy, and exoplanets, and AGN feedback.

Rachel Morgan is an optical scientist at the SETI Institute/NASA Ames Research Center. She specializes in applying integrated photonics technology to astrophysics instrumentation. She received her BS, MS, and PhD degrees in aerospace engineering in 2018, 2020, and 2023, respectively. Her PhD thesis focused on germanium-on-silicon integrated photonics for the mid-wave infrared wavelength range.

Kevin Sims is a project manager in the Space Biosciences Division at NASA Ames Research Center where he serves as the project manager of the AstroPIC project. He earned his BS degree in biomedical engineering from the University of Texas at Austin and is a certified project management professional (PMP). Supporting NASA since 2012, he is experienced in project management, flight payload development, technology demonstrations, and flight operations.

Carson Valdez received his BS degree in electrical and computer engineering from the University of California, San Diego, in 2020 with specializations in optics and electronic devices and materials, and his PhD in electrical engineering from Stanford University in 2026, specializing in integrated photonics and programmable photonics. His research interests include integrated photonics for signal processing and sensing applications.

Anne Kroo is a PhD candidate at Stanford University. Her research interests include integrated photonic circuits, structured light, optical communication, and optical sensing for applications in astrophysics and environmental monitoring.

Olav Solgaard joined Stanford University in 1999 and is now the Robert L. and Audrey S. Hancock Professor of Electrical Engineering. His research interests include optical MEMS, silicon photonics, optical sensors, and dielectric laser accelerators. He has authored more than 500 technical publications and holds 85 patents. He is a fellow of the IEEE, the Optical Society of America, the Royal Norwegian Society of Sciences and Letters, and the Norwegian Academy of Technological Sciences.

David A. B. Miller is the W. M. Keck Professor of Electrical Engineering Emeritus at Stanford University. His interests include nanophotonics, programmable photonics, and optics fundamentals. He has published more than 300 papers, two textbooks, and more than 75 patents. He has received several awards and two honorary doctorates, is a fellow of AAAS, APS, OSA, IEEE, the Electromagnetics Academy, and the Royal Societies of London and Edinburgh, and is a member of the US National Academies of Sciences and Engineering.